

# Terahertz digital holography using angular spectrum and dual wavelength reconstruction methods

Martin S. Heimbeck,<sup>1,2,\*</sup> Myung K. Kim,<sup>3</sup> Don A. Gregory,<sup>2</sup>  
and Henry O. Everitt<sup>1</sup>

<sup>1</sup>Army Aviation and Missile RD&E Center, Weapon Sciences Directorate, Redstone Arsenal, Alabama 35898, USA

<sup>2</sup>University of Alabama in Huntsville, Department of Physics, Huntsville, Alabama 35899, USA

<sup>3</sup>University of South Florida, Department of Physics, Tampa, Florida 33620, USA

\*martin.heimbeck@us.army.mil

**Abstract:** Terahertz digital off-axis holography is demonstrated using a Mach-Zehnder interferometer with a highly coherent, frequency tunable, continuous wave terahertz source emitting around 0.7 THz and a single, spatially-scanned Schottky diode detector. The reconstruction of amplitude and phase objects is performed digitally using the angular spectrum method in conjunction with Fourier space filtering to reduce noise from the twin image and DC term. Phase unwrapping is achieved using the dual wavelength method, which offers an automated approach to overcome the  $2\pi$  phase ambiguity. Potential applications for nondestructive test and evaluation of visually opaque dielectric and composite objects are discussed.

© 2011 Optical Society of America

**OCIS codes:** (110.6795) Terahertz imaging; (090.1995) Digital holography (120.2880) Holographic interferometry.

---

## References and links

1. G. Shen, and R. Wei, "Digital holography particle image velocimetry for the measurement of 3Dt-3c flows," *Opt. Lasers Eng.* **43**(10), 1039–1055 (2005).
2. M. K. Kim, "Tomographic three-dimensional imaging of a biological specimen using wavelength-scanning digital interference holography," *Opt. Express* **7**(9), 305–310 (2000).
3. B. Kemper, and G. von Bally, "Digital holographic microscopy for live cell applications and technical inspection," *Appl. Opt.* **47**(4), A52–A61 (2008).
4. W. Xu, M. H. Jericho, I. A. Meinertzhagen, and H. J. Kreuzer, "Digital in-line holography for biological applications," in *Proceedings of the National Academy of Science USA*, (PNAS, 2001) pp. 11301–11305.
5. G. Popescu, L. P. Deflores, J. C. Vaughan, K. Badizadegan, H. Iwai, R. R. Dasari, and M. S. Feld, "Fourier phase microscopy for investigation of biological structures and dynamics," *Opt. Lett.* **29**(21), 2503–2505 (2004).
6. P. Marquet, B. Rappaz, P. J. Magistretti, E. Cuhe, Y. Emery, T. Colomb, and C. Depeursinge, "Digital holographic microscopy: a noninvasive contrast imaging technique allowing quantitative visualization of living cells with subwavelength axial accuracy," *Opt. Lett.* **30**(5), 468–470 (2005).
7. D. Carl, B. Kemper, G. Wernicke, and G. von Bally, "Parameter-optimized digital holographic microscope for high-resolution living-cell analysis," *Appl. Opt.* **43**(36), 6536–6544 (2004).
8. X. Song, Z. Tang, and H. Wang, "Simple and robust digital holography for phase imaging of microstructure," *Proceedings of IEEE, Control and Decision Conference (IEEE, 2009)*, pp.4656–4658.
9. L. Xu, X. Peng, J. Miao, and A. K. Asundi, "Studies of digital microscopic holography with applications to microstructure testing," *Appl. Opt.* **40**(28), 5046–5051 (2001).
10. G. Coppola, S. De Nicola, P. Ferraro, A. Finizio, S. Grilli, M. Iodice, C. Magro, and G. Pierattini, "Characterization of MEMS structures by microscopic digital holography," *Proc. SPIE* **4945**, 71–78 (2003).
11. Z. Fan, H. Pang, W. Wang, C. Ning, and F. Guo, "Three dimensional deformation measurements with digital holography," *Proceedings of IEEE International Congress on Image and Signal Processing (IEEE, 2009)*, pp. 1–5.
12. G. Pedrini, and H. J. Tiziani, "Quantitative evaluation of two-dimensional dynamic deformations using digital holography," *Opt. Laser Technol.* **29**(5), 249–256 (1997).
13. P. Picart, J. Leval, D. Mounier, and S. Gougeon, "Some opportunities for vibration analysis with time averaging in digital Fresnel holography," *Appl. Opt.* **44**(3), 337–343 (2005).

14. E. Cuche, P. Marquet, and C. Depeursinge, "Simultaneous amplitude-contrast and quantitative phase-contrast microscopy by numerical reconstruction of Fresnel off-axis holograms," *Appl. Opt.* **38**(34), 6994–7001 (1999).
15. G. L. Chen, C. Y. Lin, M. K. Kuo, and C. C. Chang, "Numerical reconstruction and twin-image suppression using an off-axis Fresnel digital hologram," *Appl. Phys. B* **90**(3-4), 527–532 (2008).
16. L. Yu, and M. K. Kim, "Wavelength-scanning digital interference holography for tomographic three-dimensional imaging by use of the angular spectrum method," *Opt. Lett.* **30**(16), 2092–2094 (2005).
17. C. J. Mann, L. Yu, C.-M. Lo, and M. K. Kim, "High-resolution quantitative phase-contrast microscopy by digital holography," *Opt. Express* **13**(22), 8693–8698 (2005).
18. [www.virginiadiodes.com](http://www.virginiadiodes.com)
19. [www.zomega-terahertz.com](http://www.zomega-terahertz.com)
20. K. B. Cooper, R. J. Dengler, N. Llombart, T. Bryllert, G. Chattopadhyay, E. Schlecht, J. Gill, C. Lee, A. Skalare, I. Mehdi, and P. H. Siegel, "Penetrating 3-D Imaging at 4- and 25-m Range Using a Submillimeter-Wave Radar," *IEEE Trans. Microw. Theory Tech.* **56**(12), 2771–2778 (2008).
21. J. Pearce, H. Choi, D. M. Mittleman, J. White, and D. Zimdars, "Terahertz wide aperture reflection tomography," *Opt. Lett.* **30**(13), 1653–1655 (2005).
22. A. Tamminen, J. Ala-Laurinaho, and A.V. Räsänen, "Indirect holographic imaging: evaluation of image quality at 310 GHz," *Proc. SPIE* **7670**, A1–A11 (2010).
23. A. A. Gorodetsky, and V. G. Bespalov, "THz computational holography process & optimization," *Proc. SPIE* **6893**, F1–F9 (2008).
24. R. J. Mahon, J. A. Murphy, and W. Lanigan, "Digital holography at millimetre wavelengths," *Opt. Commun.* **260**(2), 469–473 (2006).
25. Y. Zhang, W. Zhou, X. Wang, Y. Cui, and W. Sun, "Terahertz Digital Holography," *Strain* **44**(5), 380–385 (2008).
26. A. A. Gorodetsky, and V. G. Bespalov, "THz pulse time-domain holography," *Proc. SPIE* **7601**, 71–76 (2010).
27. J. Gass, A. Dakoff, and M. K. Kim, "Phase imaging without  $2\pi$  ambiguity by multiwavelength digital holography," *Opt. Lett.* **28**(13), 1141–1143 (2003).
28. Attempts to collimate the beam using plastic lenses made of polytetrafluoroethylene (PTFE) and high-density polyethylene (HDPE) showed undesirable Fabry-Perot effects between the lens surfaces, causing significant phase noise in the hologram.
29. J. W. Goodman, *Introduction to Fourier Optics*, 3rd ed. (Roberts & Company Englewood, Greenwood Village, Colorado, 2005).
30. U. Schnars, T. M. Kreis, and W. P. O. Jüpner, "Digital recording and numerical reconstruction of holograms: reduction of the spatial frequency spectrum," *Opt. Eng.* **35**(4), 977–982 (1996).
31. J. H. Massig, "Digital off-axis holography with a synthetic aperture," *Opt. Lett.* **27**(24), 2179–2181 (2002).
32. S. A. Alexandrov, T. R. Hillman, T. Gutzler, and D. D. Sampson, "Synthetic aperture fourier holographic optical microscopy," *Phys. Rev. Lett.* **97**(16), 168102 (2006).
33. V. Mico, Z. Zalevsky, P. García-Martínez, and J. García, "Superresolved imaging in digital holography by superposition of tilted wavefronts," *Appl. Opt.* **45**(5), 822–828 (2006).
34. C. Liu, Z. Liu, F. Bo, Y. Wang, and J. Zhu, "Super-resolution digital holographic imaging method," *Appl. Phys. Lett.* **81**(17), 3143 (2002).
35. B. A. Knyazev, V. S. Cherkassky, Y. Y. Choporova, V. V. Gerasimov, M. G. Vlasenko, M. A. Dem'yanenko, and D. G. Esaev, "Real-Time Imaging Using a High-Power Monochromatic Terahertz Source: Comparative Description of Imaging Techniques with Examples of Application: Journal of Infrared Millimeter Terahertz Waves (online-only) (2011).
36. W. L. Chan, M. L. Moravec, R. G. Baraniuk, and D. M. Mittleman, "Terahertz imaging with compressed sensing and phase retrieval," *Opt. Lett.* **33**(9), 974–976 (2008).
37. C. F. Cull, D. A. Wikner, J. N. Mait, M. Mattheiss, and D. J. Brady, "Millimeter-wave compressive holography," *Appl. Opt.* **49**(19), E67–E82 (2010).
38. M. K. Kim, L. Yu, and C. J. Mann, "Interference techniques in digital holography," *J. Opt. A, Pure Appl. Opt.* **8**(7), S518–S523 (2006).
39. [www.mathworks.com](http://www.mathworks.com)

## 1. Introduction

Digital holography at optical wavelengths has been heavily developed over recent years because of newly-available high-resolution CCD cameras and advances in digital and automated image processing techniques [1]. Compelling advantages of digital holography over conventional holography include the ability to perform Fourier transforms and spectral filtering without the need for additional optical components and the simplicity by which reconstruction data may be interpreted quantitatively. Optical digital holography applications are manifold and include biological microscopy [2–7], metrology of microstructures [8–10], and deformation and vibration analysis [11–13]. Previously identified advantages of optical wavelength off-axis digital holography over in-line holography include the separation of

amplitude and phase information [14], noise reduction [15], and object focusing [16], as well as the ability to quantify optical thickness and refractive index variations of an object with sub-wavelength accuracy [17].

The recent commercial availability of terahertz (THz) sources and detectors has fostered tremendous interest in applications of THz imaging methods [18,19]. The THz region (~0.3 – 10 THz), which lies between the microwave and infrared (IR) regions, manifests advantages of both: the former penetrates many materials such as polymers and composites but provides poor spatial resolution, while the latter provides high resolution but is mostly restricted to image surfaces. Terahertz imaging provides a unique opportunity to take IR-like high-resolution imagery using RADAR-like techniques, including imagery of objects visually obscured by most dielectric materials. Furthermore, THz radiation is completely harmless, a significant advantage over X-ray imaging widely used for non-destructive testing. Consequently, a frequency modulated continuous wave (CW) THz system has already been developed into a prototype THz RADAR [20], while pulsed THz-time domain (THz-TD) techniques in a confocal imaging geometry have been used to perform THz tomography [21]. Confocal THz imaging with a single detector requires either steering the THz beam with a fast scanning mirror or scanning the object in the THz beam focal plane if the beam must remain stationary. Active imaging scenarios generally avoid broad illumination of the object because THz systems are usually power-starved, employ only one detector, and need to avoid coherent effects that degrade image quality. THz holography is an exception to this rule, and early simulations and experiments have explored these principles by producing low-resolution millimeter wave and THz amplitude holograms and pseudo-holograms using CW techniques [22–24] and THz-TD techniques [25,26], respectively.

Here we adapt dual-wavelength digital holographic methods - which have been shown to eliminate reconstruction ambiguities, improve image resolution, reduce coherent noise, and provide quantitative measurements of physical thickness, surface, and refractive index variations - in the THz region [16,27] to reconstruct amplitude and phase objects using highly coherent, monochromatic THz radiation. Such high fidelity images illustrate the potential of THz holography for non-destructive testing and evaluation of visually opaque materials and structures.

## 2. Experiment

The THz transmission holography system shown in Fig. 1(a) is based on a Mach-Zehnder interferometer. The highly coherent, frequency tunable 0.66 – 0.76 THz source is composed of a 8-20 GHz Micro Lambda Wireless microwave synthesizer operating between 13.5 and 16.0 GHz and a Virginia Diodes, Inc. multiplier chain of four frequency doublers and one tripler (48x). The source generates ~50  $\mu$ W, which is collimated by a 90 degree off-axis paraboloidal mirror to a diameter of approximately 90 mm [28]. A wire grid beam splitter (BS) divides the beam into reference and object beams. The amplitude or phase object is illuminated in transmission mode, and the diffracted object wave interferes with the reference wave following another beam splitter to recombine both beams. This second beam splitter is tilted to introduce the off-axis angle  $\theta$  between the object and reference beams. The beam splitters also allow the relative beam intensities to be adjusted since amplitude objects generally require a stronger object beam than phase objects. However, a strong reference beam is also desirable as it relaxes the minimum reference angle required to separate the real and virtual images containing the object wavefield information from the on-axis “DC” term [29].

The VDI Schottky diode square law detector spans 0.60 – 0.90 THz with a responsivity of ~1000 V/W and uses a 26 dB gain diamond aperture horn with a –3dB full beamwidth of 10 degrees. The detector output voltage is filtered and amplified by a SR560 low-noise voltage preamplifier and acquired in LabVIEW with a National Instruments USB 6251DAQ. During the acquisition of phase holograms, a 7270 Signal Recovery lock-in amplifier was added

between the SR560 and the USB 6251DAQ to improve the signal to noise ratio. A THz image is recorded by scanning the single THz detector across the hologram plane with two motorized Zaber linear stages in an X-Y translation configuration. The maximum off-axis angle, and resulting maximum fringe frequency, is limited by the spatial cutoff frequency of the THz detector horn. For our system, the maximum resolvable spatial frequency  $f_c$  of the interference pattern formed by the object and reference was found to be 0.51 cycles/mm for a 0.712 THz beam ( $\lambda = 0.4213$  mm). Figure 1(b) shows a 100 x 100 mm interferogram from the interfering object and reference waves. The maximum off-axis angle  $\theta_{max}$  between the two beams is therefore

$$\theta_{max} = \sin^{-1}(f_c \cdot \lambda), \quad (1)$$

which is 12.41 degrees in this experiment. Customized detector horns with optimized gain and antenna pattern characteristics may be able to resolve higher spatial frequencies and allow for larger off-axis angles, improving the separability of the real and imaginary images from the DC term. Other methods to increase image resolution, such as hologram magnification or super resolution techniques, may be necessary in the future as an intermediate step between THz hologram generation and recording [30–34].

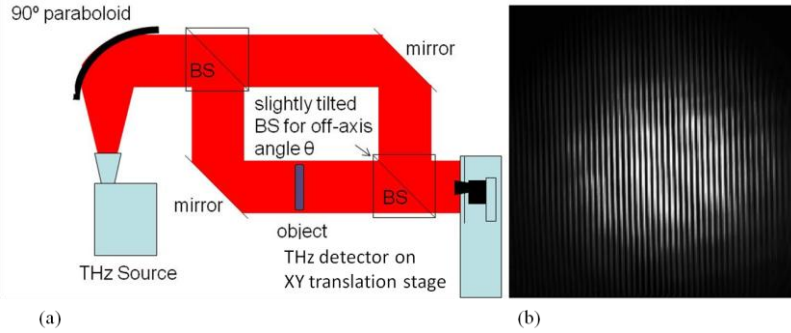


Fig. 1. THz digital holography experimental configuration (a) and a typical interferogram at detector/hologram recording plane (b).

The maximum resolvable spatial frequency bandwidth  $B$  of an object required to ensure isolation of the real and imaginary images from the DC term is  $B = \sin\theta_{max}/(3\lambda)$ , which can be relaxed to  $B = \sin\theta_{max}/\lambda$  if the reference wave is much stronger than the object wave [29]. The intensity pattern  $I(x,y)$  recorded by the scanning detector is described by the well-known relationship of two interfering waves: the object wave  $O(x,y)$  and reference wave  $R(x,y)\exp(-j2\pi\eta y)$ , where  $\eta$  is related to the off-axis angle  $\theta$  by  $\eta = \sin\theta/\lambda$  [28]. Here,  $\theta$  is chosen to lie in a plane defined by the y-coordinate (in the recording plane) and the z-coordinate (normal to the recording plane). The total recorded pattern in the x-y hologram plane is written as

$$I(x,y) = |O(x,y)|^2 + |R(x,y)|^2 + O(x,y)^* R(x,y)\exp(-j\eta 2\pi y) + O(x,y) R(x,y)^* \exp(j\eta 2\pi y). \quad (2)$$

Performing a two dimensional Fourier transform  $F\{I(x,y)\}$  results in the spatial frequency spectrum of  $I(x,y)$  containing four Fourier spectra corresponding to the four terms in Eq. (2), which can be abbreviated as  $O^2 + R^2 + O^*R + OR^*$ .  $|F\{O^2\}|$  represents the autocorrelation of  $O$ , whose spectrum has twice the bandwidth ( $2B$ ) of  $O$  and is located symmetrically around the origin  $f_x f_y = 0$ .  $|F\{R^2\}|$  is a delta function located at  $f_x f_y = 0$ , assuming  $R$  is a plane wave.  $|F\{O^*R\}|$  contains the spectrum of the real image of  $O$  and is located symmetrically around  $f_x = 0, f_y = -\eta$ . Similarly,  $|F\{OR^*\}|$  contains the spectrum of the virtual image of  $O$  and is located symmetrically around  $f_x = 0, f_y = \eta$ . Figure 2(a) illustrates the locations of the four spectra for the case where the spectra can be fully separated. Figure 2(b) considers the approximation

where the reference wave is much stronger in magnitude than the object wave, in which case  $F\{O^2\}$  becomes negligible.

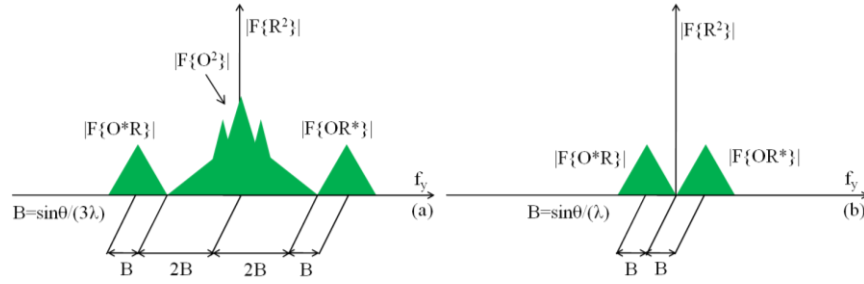


Fig. 2. Illustration of separable Fourier spectra using off-axis holography for small (a) and large (b) reference signals.

### 3. Sampling

One of the compelling advantages for digital holography using CCDs is the quantitative ability to record three-dimensional amplitude and phase information of an entire object in real time. Although under development [35], the present lack of suitable high-resolution THz focal plane arrays, however, requires a THz detector to be scanned across the image plane to record the hologram. Depending on the image size, pixel resolution, and integration time required, the total scan time to acquire a hologram can take several hours. Computationally supported efficient sampling techniques such as compressive sampling may mitigate the scan time somewhat [36,37]. Although the scanning stages and optical system must still exhibit sufficient precision and alignment over long-duration scans, the sub-millimeter wavelength of THz radiation allows the use of economical long-travel linear stages and does not require vibration isolation on an air platform during measurements. A more challenging requirement is that the THz source remains temporally and spatially coherent over the acquisition time. The THz source used in this experiment did not exhibit any notable instability in its coherence, even over several days of continuous operation.

As previously mentioned, the image resolution is determined by the resolution of the detector. The antenna pattern of the THz detector follows a Gaussian curve as depicted in Fig. 3. It has a  $-3\text{dB}$  full beamwidth of 10 degrees. Therefore, the maximum introducible off axis angle  $\theta_{max}$  is both a function of the angular antenna pattern and the detector's cutoff frequency. The optical transfer function (OTF) of the detector with aperture horn width of  $w = 2$  mm is symmetric in  $y$  and  $x$  coordinates and is related to its Fourier transform by [29]

$$\text{OTF} \propto \left| \mathcal{F} \left\{ \text{rect} \left( \frac{y}{w} \right) \right\} \right|^2 \propto \text{sinc}^2 (w \cdot f_y). \quad (3)$$

The cutoff frequency  $f_c$  of the detector occurs where the OTF has its first zero, which is  $f_c = 1/w = 0.50$  cycles/mm, producing an off-axis angle of  $\theta_{max} = 12.40$  degrees. At this angle, the fringe amplitude is reduced to approximately 27% of its peak value due to the antenna horn pattern as shown in Fig. 3. Nyquist sampling requires the detector be scanned with  $\sim 0.5$  mm steps, but to take advantage of sub-wavelength depth resolution using this interferometric technique, a scan step of 0.2 mm was rarely exceeded.

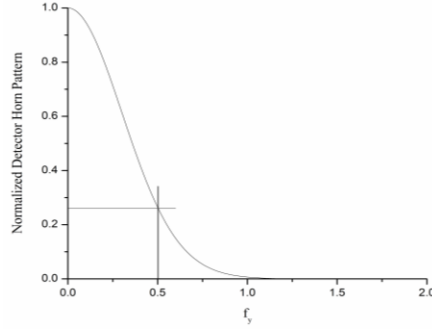


Fig. 3. THz detector horn pattern as a function of spatial frequency  $f_x, f_y$ ; the THz signal captured by the horn antenna at the off-axis angle  $\theta_{max}$  corresponding to a spatial frequency 0.5 cycles/mm is reduced to 27% of its peak value.

#### 4. Reconstruction process

Commonly used Fresnel holographic reconstruction methods require only one Fourier transform, but this approximation imposes certain conditions - such as a minimum object-hologram plane distance - that limit its applicability [38]. A slightly more computationally demanding but significantly more accurate method of reconstruction is the angular spectrum method [38]. Although it requires a second Fourier transform, this adds only minor processing time for digital reconstruction if the fast Fourier transform (FFT) algorithm is used (e.g. Matlab is used here [39]).

The angular spectrum  $A(\alpha/\lambda, \beta/\lambda, z)$  of a wavefield  $O(x, y, z)$  in the transverse  $x$ - $y$  plane propagating in the  $z$  direction is the two dimensional Fourier transform of  $O(x, y, z)$ . The direction cosines  $\alpha$  and  $\beta$  are directly related to the spatial frequencies  $f_x, f_y$  of the Fourier transform by  $\alpha = \lambda f_x$  and  $\beta = \lambda f_y$ . The recorded hologram chosen at  $z = 0$  provides the wavefield  $U(x, y, z = 0)$ .  $A(\alpha/\lambda, \beta/\lambda, z = 0)$  is then readily computed with a FFT. The angular spectrum at any other location of  $z$  can be found by multiplying  $A(\alpha/\lambda, \beta/\lambda, z = 0)$  with a propagation kernel [29]:

$$\mathbb{A}\left(\frac{\alpha}{\lambda}, \frac{\beta}{\lambda}, z\right) = \mathbb{A}\left(\frac{\alpha}{\lambda}, \frac{\beta}{\lambda}, 0\right) \exp\left(j \frac{2\pi}{\lambda} \sqrt{1 - \alpha^2 - \beta^2} z\right). \quad (4)$$

Usually,  $z$  is chosen to be the object – hologram plane distance, but any location of  $z$  can be chosen. If the object – detector plane distance is unknown, it can be found by varying  $z$  until the reconstructed object is in focus. The original object wavefield  $U(x, y, z)$  is then computed with another FFT, this time of  $A(\alpha/\lambda, \beta/\lambda, z)$ .

The previously described steps do not include Fourier space filtering. Assuming the off-axis angle is sufficiently large to separate the frequency spectrum of the real object wavefield from the DC term (Fig. 2),  $A(\alpha/\lambda, \beta/\lambda, z)$  can be multiplied by a filter that rejects the twin image and DC spectra. Here the filter is a rectangular or circular array of zeroes wherever the spectra is to be rejected and ones wherever the spectra of the real image is located. In optical holography, the hologram must be illuminated by the same reference wave in order to form a real or virtual image. The digital reconstruction process requires the same and can be approached digitally. The hologram is multiplied by the reference wave described by

$$R(\theta) = \exp\left(j \frac{2\pi}{\lambda} y \cdot \sin\theta\right), \quad (5)$$

where the off axis angle  $\theta$  is assumed in the  $y$ - $z$  plane. The filtered version of  $A(\alpha/\lambda, \beta/\lambda, z = 0)$ , which at this point should contain only the frequency content of the real wavefield, is then back-propagated using Eq. (4), after which another FFT reproduces the original object wavefield  $U(x, y, z)$ . In summary, the cascaded steps to find  $U(x, y, z)$  are

$$U(x, y, z) = \text{iFFT}\left\{\text{backpropagation}\left(\text{filtering}\left(\text{FFT}\{U(x, y, 0)\}\right)\right)\right\}, \quad (6)$$

where iFFT means inverse FFT.

Additional work is required to overcome the well-known  $2\pi$  phase ambiguity when reconstructing phase objects. Which method is used to unwrap the phase image depends on the type of THz source and detector used, and we used dual wavelength holography because our highly coherent THz source can be frequency tuned over tens of GHz. It has been demonstrated at optical wavelengths [27] that the wavelength, and therefore the  $2\pi$  phase step, can be extended arbitrarily to a new optical thickness or beat wavelength  $\lambda_b$  as long as the hologram can be recorded at two wavelengths  $\lambda_1$  and  $\lambda_2$  such that

$$\lambda_b = \frac{\lambda_1 \cdot \lambda_2}{|\lambda_2 - \lambda_1|}. \quad (7)$$

The phase values of the two phase images corresponding to  $\lambda_1$  and  $\lambda_2$  range between  $-\pi$  and  $\pi$ . Following the procedure described in [27], the two phase images are subtracted. The phase values of the new phase map range between  $-2\pi$  and  $2\pi$ . Adding  $2\pi$  wherever the phase map  $< 0$  results in a new phase map that is free of  $2\pi$  discontinuities over the range of the beat wavelength. The remaining step is to convert the phase map profile into an optical thickness profile, achieved by multiplying the phase map by the beat frequency and dividing it by  $2\pi$ .

## 5. Results

The experimental setup illustrated in Fig. 1(a) was used to record amplitude and phase holograms at frequencies around 0.7 THz. Figure 4(a–d) illustrates the reconstruction process of an amplitude object recorded at 0.712 THz. The thin 30 x 30 mm metallic object shown in Fig. 4(a) was entirely illuminated by the object beam. The structure was imaged at a distance of 200 mm and had a series of holes with diameters ranging from 2.0 mm to 0.4 mm. A resolution limit based on diffraction and Rayleigh's criterion can be formulated that states that two neighboring object points can just be resolved if their angular separation  $\omega = 1.22 \lambda/D$  where  $D$  is the diameter of the objective aperture. Here, for  $D = 80$  mm  $\omega = 0.0064$ , which is equivalent to a lateral object point separation of 0.64 mm at a object – detector distance of 200 mm. The upper row of holes on the object containing three holes of diameters from 1.5 mm to 2.0 mm are sufficiently separated from each other to satisfy this resolution limit and are therefore clearly visible in Fig. 4(d). The second row of holes contains a set of nine 0.9 mm diameter holes arranged horizontally. These holes are separated 0.9 mm from each other horizontally but only 0.4 mm vertically from the third row of holes. Therefore, the diffraction limit is satisfied horizontally but not vertically, which is evident in Fig. 4(d) showing that the nine holes are indicated in the horizontal direction but smear together with the third row of holes in the vertical direction. The subsequent rows of holes range in diameter from 0.8 – 0.4 mm from top to bottom. Although the four holes on the bottom row are only about the size of the wavelength, they are horizontally separated at about 1.0 mm from each other, which makes them distinguishable in the horizontal direction as their separation satisfies the diffraction limit. Clearly, the spatial resolution of the amplitude reconstruction is determined by diffraction, not by the maximum spatial frequency of 0.5 cycles/mm or the 2 x 2 mm detector aperture.

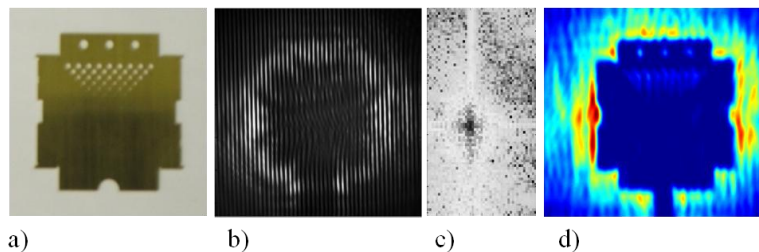


Fig. 4. Steps in the reconstruction of the amplitude object at 0.712 THz: photograph (a), 80 x 80 mm hologram (b), filtered spectrum of real image (c), and amplitude reconstruction (d).

The previously mentioned ability to reconstruct the object wave at any distance  $z$  to obtain digital object focusing is illustrated in Fig. 5. By varying the object-hologram distance  $z$  in the propagation kernel of Eq. (6) the object-detector distance could be ascertained to be  $200 \pm 5$  mm which agreed with the measured value of 200 mm.

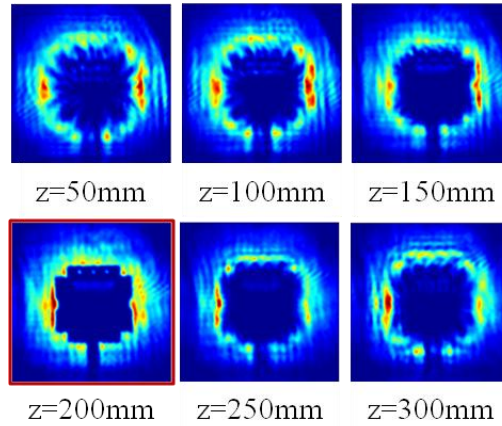


Fig. 5. Digital object focusing to find the object-detector distance  $z$ . The best focus is near  $z = 200$  mm.

Next, two-wavelength optical phase unwrapping was used to obtain a holographic image of the plano-convex polymethylpentene (PMP) lens shown in Fig. 6(a) used to deduce index variations in the material. Its physical size was 52.0 mm in diameter and the physical thickness variation from the edge to the center of the lens was  $h_c = 2.0 \pm 0.01$  mm, which was measured with a caliper. Figures 6(b,c) show the recorded holograms at 680.0 and 725.0 GHz, corresponding to the wavelengths of  $\lambda_1 = 0.4418$  mm and  $\lambda_2 = 0.4438$  mm, respectively. The scanned field of view is 80 x 80 mm with 400 x 400 pixels. Each hologram is processed using the angular spectrum method (at reconstruction distance of 280 mm) to obtain the amplitude (Figs. 6(d,e)), and phase (Figs. 6(f,g)) images shown, where the gray scale of the phase images spans the range of  $-\pi$  to  $+\pi$ . The two phase profiles are combined, according to the procedure described above, to yield the unwrapped phase profile in Fig. 6(h), and rendered in pseudo-3D perspective view in Fig. 6(j). Figure 6(i) shows a side view through the middle of the unwrapped phase map, where the vertical scale is in radians. The optical path difference (OPD) between the edge and center of the lens resulted in a phase difference of  $0.89 \pm 0.10$  radians according to the hologram reconstruction corresponding to an OPD of  $2.92 \pm 0.10$  mm. Therefore, the refractive index  $n = 1.46 \pm 0.01$  of the lens material could be ascertained from the OPD according to the hologram reconstruction and the physical thickness variation according to the caliper measurement. A refractive index of 1.46 is typical for PMP at THz frequencies while variations at the second decimal are a known quality issue for polymer lenses. Figure 6(i) also illustrates that a subwavelength thickness resolution of about  $10 \mu\text{m}$  ( $\lambda/40$  at 725 GHz) was obtained. The lens's edge thickness of  $10.70 \pm 0.01$  mm according to the caliper measurement is larger than one beat wavelength but less than  $2\lambda_b$ . Therefore, the phase floor of approximately  $-1.30$  radians outside the lens (Fig. 6(i)) corresponds to  $-1.50 \times 2\pi = -9.40$  radians considering the phase reversal at approximately  $-4.30$  radians. Therefore, the lens thickness at the edge can be estimated as  $(8.8 - 4.3)/2\pi \times \lambda_b/(n-1) = 10.20 \pm 1.00$  mm, which is in excellent agreement with the measured value considering the previously mentioned variations in the refractive index. The cause for index variations in lens materials can be due to several factors including density variations in the material as well as birefringence effects. In fact, the reconstruction shows several interesting features in the lens that are not physically present on the surface of the lens. Beyond the

obvious diffraction rings, the reconstruction (Fig. 6(j)) exhibits a cross-shaped area (yellow color) in the center of the lens typical of plates and lenses that exhibit birefringence. The remaining irregularities may be contributed by aliasing in the scanning mechanism, diffraction from other optics, and the spatial quality of the THz beam itself.

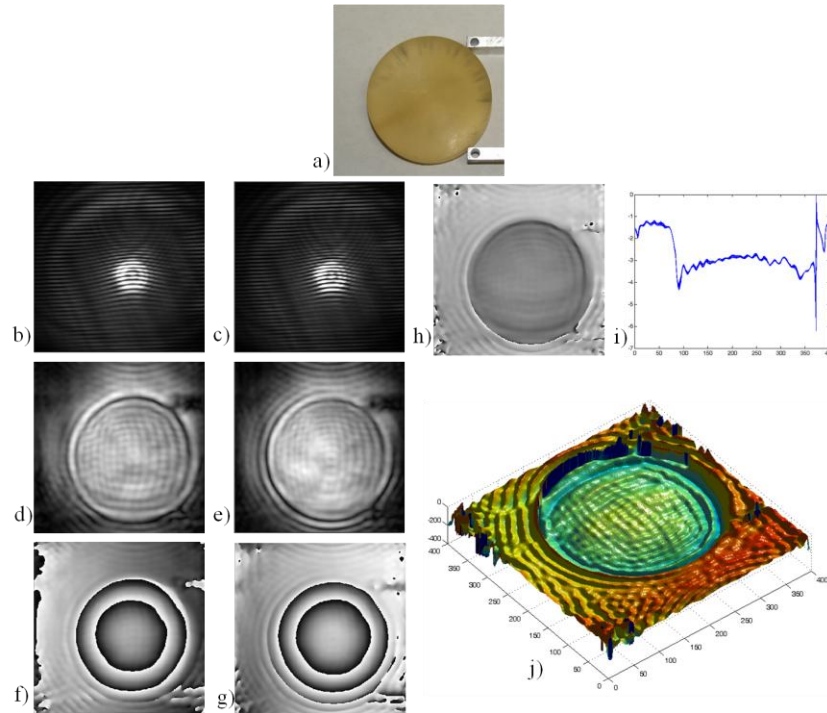


Fig. 6. Steps in the reconstruction of the phase object using dual wavelength reconstruction: photograph (a), holograms at 680 and 725 GHz (b-c), amplitude reconstructions (d-e), phase reconstructions (f-g), unwrapped reconstruction (h), cross-section through center of unwrapped reconstruction (i), pseudo 3D perspective of the unwrapped reconstruction (j).

Once fully optimized, a clear application for THz digital holography is in the field of nondestructive test and evaluation. Any relatively thin object that is transparent to THz radiation could be imaged with sub-wavelength axial resolution using a modest power, continuous wave THz source. For example, amplitude reconstructions may reveal wiring defects on multi-layer circuit boards, whereas phase reconstructions can reveal inhomogeneities in dielectrics. Current strides to develop THz focal plane arrays would further expand possible applications to include one-shot or short duration events such as vibration analysis and stress-induced birefringence.

## 6. Conclusion

In summary, we have recorded and reconstructed digital THz holograms of amplitude and phase objects at a resolution limited by the OTF of the detector area and spacing. Lateral image resolution after reconstruction is comparable to highly focused confocal imagers, while the axial resolution is about  $\lambda/40$ . The dual wavelength reconstruction process allows for the reconstruction and analysis of visually opaque phase objects that are many wavelengths thick.